Northern Chile intermediate-depth earthquakes controlled by plate hydration

Leoncio Cabrera, Sergio Ruiz, Piero Poli, Eduardo Contreras-Reyes, Axel
Osses, Renzo Mancini

Northern Chile Intermediate-Depth Earthquakes Controlled by Plate Hydration

Leoncio Cabrera[1]†, Sergio Ruiz[1], Piero Poli[2], Eduardo Contreras-Reyes[1], Axel Osses[3] and Renzo Mancini[1]

[1]Departamento de Geofísica, Facultad de Ciencias Físicas y Matemáticas, Universidad de Chile.

[2]ISTerre Institut des Sciences de la Terre, CNRS, Université Grenoble Alpes.

[3]Departamento de Ingeniería Matemática y Centro de Modelamiento Matemático UMI 2807 CNRS, Facultad de Ciencias Físicas y Matemáticas, Universidad de Chile.

Corresponding author: Leoncio Cabrera (leoncio.cabrera@univ-grenoble-alpes.fr)

Université Grenoble Alpes, ISTerre CS 40700 38058, GRENOBLE Cedex 9

†Currently at ISTerre Institut des Sciences de la Terre, Université Grenoble Alpes.

16   **Abstract**

17   We investigate the variations of the seismic source properties and aftershock activity using

18   kinematic inversions and template-matching, for six large magnitude intermediate-depth

19   earthquakes occurred in northern Chile. Results show similar rupture geometry and stress drop

20   values between 7-30 MPa. Conversely, aftershocks productivity systematically decreases for the

21   deeper events within the slab. Particularly there is a dramatic decrease in aftershock activity

22   below the 400-450 ºC isotherm-depth, which separates high and low-hydrated zones. The events

23   exhibit tensional focal mechanisms at unexpected depths within the slab, suggesting a deepening

24   of the neutral plane, where the extensional regimen reaches the 700-800ºC isotherm-depth. We

25   interpret the reduction of aftershocks in the lower part of the extensional regime as the absence

26   of a hydrated-slab at those depths. Our finding highlights the role of the thermal-structure and

27   fluids in the subducting plate, in controlling the intermediated-depth seismic activity and shed

28   new light in their causative mechanism.

29

30   **Keywords:** Intraslab Intermediate Depth Earthquakes, Aftershock, Chile, Subduction, Slab.

31

32
33

1 Introduction

Rupture mechanism of intermediate-depth earthquakes (IDEs) is one of the biggest open questions in seismology (Frohlich, 2006; Houston, 2015). They occur mostly at subduction zones in the so called double seismic zones (DSZ), where two parallel seismicity planes are observed. The upper seismicity plane (USP) is inferred to occur within the subducting oceanic crust and/or the upper mantle due to dehydration reactions (Hacker et al., 2003; Kirby, 1995). In contrast, the lower seismicity plane (LSP) occurs in the lithospheric mantle, and its mechanism is still under debate (Ferrand et al., 2017; Ohuchi et al., 2017; Peacock, 2001; Reynard, 2010). Hypothesis for this process include dehydration-embrittlement of antigorite (Peacock, 2001), reactivation of pre-existing shear zones (Reynard, 2010) and quasi-adiabatic shear-heating instabilities (John et al., 2009). Furthermore, laboratory experiments also suggest that faulting at intermediate depths may occur under dry conditions (Ohuchi et al., 2017) or by dehydration-driven stress transfer under partially hydrated mantle conditions (Ferrand et al., 2017).

The DSZ is usually characterized by compressional deep events within the oceanic lithospheric mantle in trench-outer rise regions prior to subduction, while the upper part of the oceanic lithosphere is affected by a tensional regime. This stress field in the trench-outer rise region is controlled by the plate bending caused by the interplay of slab pull forces and the rheology of the oceanic lithosphere (Contrereas-Reyes & Osses, 2010). Furthermore, based on a worldwide compilation of trench outer rise earthquakes, the position of the neutral plane of the stress field within the oceanic lithosphere have been estimated to be approximately coincident with the 400º-450ºC isotherm-depth (Seno & Yamanaka, 1996). Likewise, Ruiz & Contreras-Reyes (2015) and Carrasco et al., (2019) found that tensional outer rise events are confined to the upper oceanic lithosphere to isotherm-depths shallower than 400ºC offshore central Chile. Off Japan, Kita et

57 al., (2010) reported that the transition from upper tensional to compressional intraplate

58 earthquakes occur at 22 km beneath the base of the Eurasian plate beneath Tohoku. However,

59 this transition occurs only ~10 km beneath the upper plate beneath Hokkaido. The authors

60 attribute this difference to the complexity of the oblique subduction beneath Hokkaido, and they

61 further pointed out that the stress regime is the combination of two stress fields: (i) the

62 bending/unbending force, and (ii) the thermomechanical and petrological forces.

63 Although IDEs are characterized by shear slip on faults similar as inland crustal or interplate

64 earthquakes, anomalous behavior is often observed for the first ones such as thermal-dependence

65 radiated seismic energies (Wiens, 2001), significant non-double-couple mechanisms (Richardson

66 & Jordan, 2002), and high stress drops (Frohlich, 2006; Poli et al., 2014; Houston, 2015) among

67 others. A remarkable characteristic of intermediate and deep earthquakes is their general lower

68 aftershock productivity as compared with shallower events (Frohlich, 1987; Wiens et al., 1994;

69 Zhan, 2014; Houston, 2015), although few cases with large activity exist (Wiens et al., 1994).

70 Aftershocks activity has been related to fault properties as state of stress (Shebalien & Narteau,

71 2017), rupture processes (Poli et al., 2016), seismic coupling (Hainzl et al., 2019) and the

72 thermal state of the slab, with colder slabs showing a greater number of aftershocks (Wiens &

73 Gilbert, 1996). A main issue is to understand if this general decrease in the number of

74 aftershocks is real, or it is due to the lack of near-field data (Li et al., 2018). It is thus

75 fundamental to tackle this issue, to better assess the aftershock activity (Dascher-Cousineau et

76 al., 2020) and get new insights about the mechanism(s) and physical conditions controlling the

77 occurrence of IDEs.

78 Since 2010, six intermediate-depth events with magnitudes (Mw) greater than 6 occurred in

79 northern Chile between 17ºS and 21ºS (Figure 1 and Table S1), where the Centro Sismológico

80   Nacional de la Universidad de Chile (CSN; Barrientos et al., 2018), Integrated Plate Boundary

81   Observatory Chile (IPOC; GFZ, & CNRS-INSU, 2006) and Central Andean Uplift and the

82   Geodynamics of the High Topography (CAUGHT; Beck et al., 2010) seismic networks have

83   been deployed (Figure 1a). These events are of main interest for several reasons. First, they are

84   registered by a dense network of broad-band and strong-motion sensors in the near-field

85   providing an opportunity to avoid problems with detection levels (Poli et al., 2016; Shebalien &

86   Narteau, 2017; Zhan et al., 2014). Second, the six events are located in a very limited volume,

87   reducing issues related with attenuation and other propagation effects, which are possibly

88   affecting the estimation and thus the comparison of source properties (Prieto et al., 2012).

89   Finally, their magnitudes (Mw ~ 6.3) and focal mechanisms are similar (Figure 1). We thus have

90   a unique opportunity to compare source properties and aftershock activity, with limited bias due

91   to propagation and rupture geometry. In addition, according to the CSN catalogue they exhibit

92   different aftershock productivity. For the shallowest event (E1 in Figure 1c), there are more than

93   40 aftershocks reported, including some of them with magnitude equal or greater than Mw 4.0

94   (see Supplementary Information). For the deeper ones there is a decrease in the number of

95   aftershocks with no aftershocks for the deepest event (E6 in Figure 1c).

96   To better characterize if differences in between these events exist, we study their aftershock

97   activity and rupture properties, using template matching (TM) and kinematic inversions (KI).

98   Furthermore, we developed a thermal model using the finite element method (FEM), with the

99   aim of analyze the impact of slab temperature on seismic behavior. In the next sections, the

100   tectonic setting and methodologies used in this study followed by their respective results are

101   described, and finally the discussions and conclusions are presented.

102

2 Tectonic Setting

The northern Chilean convergent margin is characterized by the subduction of the oceanic Nazca plate beneath the continental South American plate (Figure 1) at a currently convergence rate of ~67 mm/a (Khazaradze & Klotz, 2003), although the average convergence rate during the last 20 Ma is about 85 mm/a (DeMets et al. 2010). The Nazca plate in the study region (18º - 21ºS) was formed in the East Pacific Rise 45-52 Ma (Mueller et al., 2008), whereas its crustal thickness is 6-7 km thick inferred by seismic constraints (Patzwahl et al., 1999; Ranero and Sallarès, 2004; Contreras-Reyes et al., 2012; Maksymowicz et al., 2018). The northern Chilean margin has a poorly sedimented trench (< 200 m; Maksymowicz et al., 2018) due to the reduced sediment supply from the Andes in the extremely arid region of the Atacama Desert. The continental slope is steep as the frontal part of the margin lacks a well-developed frontal prism (Contreras-Reyes 2018; Maksymowicz et al., 2018).

The northern Chilean margin has undergone subduction erosion since at least the Jurassic, which is inferred from the eastward migration of the volcanic arc (e.g. Rutland, 1971; Stern, 2011) as well as the long-term arcward retreat of the trench, crustal thinning and subsidence of the outer forearc (e.g., Kukowski & Oncken 2006; Contreras-Reyes 2018). Long-term subduction rates for northern Chile have been estimated with values of 40-45 $km^3Myr^{-1}km^{-1}$ (Kukowski & Oncken 2006). On the other hand, the oceanic Nazca plate presents well developed tensional faults seen in the bathymetric data (Geersen et al., 2018), which were formed by bending of the oceanic plate (Ranero et al., 2005). These bend faults provide the pathways for seawater infiltration

123   reaching the oceanic mantle according to seismic and geodynamic studies (see Contreras-Reyes

124   & Osses, 2010 and references therein).

125

126   **3 Aftershock productivity**

127   **3.1 Detection of aftershocks using template matching**

128   The six studied IDEs have tensional focal mechanism and span a range of depth from 90 to 130

129   km (Figure 1), in a region where a double seismic zone (DSZ) has been previously reported

130   (Comte et al., 1999; Dorbath et al., 2008; Sippl et al., 2018; Florez & Prieto, 2019) and the

131   seismic catalog has magnitude of completeness ~ Ml 3.5 (Barrientos et al., 2018). It is thus likely

132   that aftershocks are missing for some the studied events, which is improved using template

133   matching (TM).

134   TM has been widely used to detect events in aftershocks sequences, where seismicity is known

135   to repeat (Shelly et al., 2007; Peng & Zhao, 2009; Frank et al., 2017; Li et al., 2018). In a similar

136   way, we here apply TM to improve the detection of aftershocks following the analyzed events

137   (Figure 1). We base our analysis on continuous three-component velocity seismological data

138   from the CSN, IPOC, and CAUGHT seismic networks, using the five nearest stations to the

139   source region of each event (Figure S15). Data were continuously recorded at a sampling rate of

140   100 Hz for IPOC and CSN stations, and 40 Hz for CAUGHT stations. To detect non-reported

141   aftershocks, we searched for events with similar waveforms to those reported as mainshock and

142   aftershocks for the CSN (template candidates, see Supplementary Information). A space-time

143   window needs to select reference events and build templates. A large window implies including

144   more events, but also more background events as well, while a smaller window decreases this

145   effect, but is more likely to miss some aftershocks. Since the six earthquakes have similar

146   characteristics such as magnitude, focal mechanism, hypocenter and station coverage, we use the

147   same spatial and temporal scale for all of them in order to preserve a homogeneous criterion that

148   allows their comparison. After some tests with different windows size and considering some

149   previous works (e.g., Persh and Houston, 2004; Dascher-Cousineau et al., 2020) we define the

150   spatial limit using a 3D radius of 25 km from each hypocenter, and 25 days of data after each

151   mainshock, as this is the maximum number of days for which the five stations closest to each

152   event were operating continuously. Both continuous data and template waveforms were bandpass

153   filtered from 5 to 10 Hz because this frequency range exhibits better signal to noise ratios, and

154   decimated to 25 Hz. To select high-quality template events, we follow Frank et al. (2017) and we

155   estimate the signal-to-noise ratio (SNR) on the vertical component as the ratio between the RMS

156   velocity during the first 25 s of the P-wave and the RMS velocity during a 25 s of noise before

157   the P-wave arrival time. Only template candidates with SNR > 5 in at least 3 stations are used as

158   templates. We define the resulting template waveforms as 30 s time windows that start 5 s before

159   event's P-wave arrival at each station. Then we calculate the correlation coefficients between

160   template waveforms and continuous data in a sliding window that preserves the seismic

161   moveouts (Frank et al., 2017), to get a time series that represents the similarity of the continuous

162   data to the matched-filter template. We search sample-by-sample considering a detection

163   threshold that is 10 times the median absolute deviation (MAD) of the correlation sum to detect

164   event significantly similar to the template. Events detected with this criterion, are then

165   considered to occur at the same hypocenter (determined by the CSN) as their template, and we

166   estimate their magnitude by computing the median amplitude ratio between the template event

167   and the aftershock over the 5-station network, assuming that a tenfold increase in amplitude

168   corresponds to one unit increase in magnitude. Figures 2b-c show an example for E2 and E5,

169   where using the mainshocks waveforms as templates, two new detections with inferred

170   magnitudes (Mw) of 1.8 and 2.7 occurred four days (for E2) and some hours (for E5) after

171   mainshocks.

172   To avoid redundancy of events detected by multiple templates, we remove detections within 30 s

173   of another detections, by keeping the event with the highest network correlation coefficient.

174   Finally, we use the new catalogue (including CSN and new detected aftershocks) as templates

175   candidates, and the process is repeated once.

176   **3.2 Aftershock Activity**

177   Figure 3a shows all new detections and catalog events, for 25 days after each mainshock. As is

178   common for aftershock sequences, the number of events decreases over time, with a higher

179   concentration close to the mainshock. On the other hand, the number of aftershocks shows a

180   clear reduction as function of depth, down to E6 that is showing no aftershocks (Figures 3a-c).

181   The most productive event is E1, located just ~7 km from the top of slab (Figure 1). For this

182   earthquake, we used 45 events as templates, and we found 2044 aftershocks, nearly 47 times

183   more.

184   It is important to highlight that there are no aftershocks reported in the CSN catalog for E2, E5,

185   and E6. For these events, we use the mainshock waveforms for detection. This strategy permits

186   to find new events for E2 and E5, suggesting that the sole main event waveforms can improve

187   the detection. Figure 2 shows an example of detections for E2 and E5 using mainshock

188   waveforms as templates (see Table S2 for more details about detections). According to the

189   above, lack of detection seen for E6 is a robust feature of our analysis.

190

191   **4 Thermal structure**

192   **4.1 Thermal-Fluid Numerical Model**

193   To assess the thermal conditions at the depth of the analyzed events, we developed a 2D-thermal

194   model using Finite Element Method (FEM) for northern Chile, along the BB' profile (Figure 1).

195   The model is constrained by the plate geometry of SLAB2.0 (Hayes et al., 2018), hypocenter

196   data, and published thermal parameters in the area (see Table S5).

197   **4.1.1 Numerical Model**

198   The thermal subduction model consists in a two-dimensional finite element discretization of a

199   coupled system of a heat equation for the temperature and and the Stokes's system for the

200   subducting lithospheric plate speed and asthenospheric fluxes. The heat equation is given by:

$$-\kappa \nabla^2 T + \vec{u} \cdot \nabla T - Q = 0 \qquad (1)$$

201   in the region of interest Ω, where T is the temperature and the first term corresponds to heat

202   diffusion where κ is the thermal diffusivity depending on space (ratio of the thermal conductivity

203   k and the thermal capacity ρc_p of the media), the second term corresponds to the heat transport

204   due to lithospheric speed and asthenospheric fluxes $\vec{u}$, and the last term stands for the external heat

205   sources such as radiogenic or frictional heat. No friction heat effects are considered in this study

206   since in the case young lithospheres the effects of friction can be neglected (Vöelker et al., 2011).

207 Thermal effects due to the subducted eroded material above the incoming/subducting lithosphere

208 are also neglected for the sake of model simplicity.

209 Given a velocity field $\vec{u}$ in the whole region Ω, we obtain the steady state temperature T as the

210 limit of T_n solution of the following variational problem discretized with Lagrange finite elements

211 of type P2 (space V_h) and iterating for $n \geq 1$ starting from $T_0 = 0$ until convergence, where Δt is

212 some fictitious numerical time step:

$$\frac{1}{\Delta t} \int_\Omega (T^n - T^{n-1})S + \int_\Omega \kappa \, \nabla T^n \cdot \nabla S + \int_\Omega (\vec{u} \cdot \nabla T^n)S - \int_\Omega QS = 0 \ \forall S \in V_h \qquad (2)$$

213 Given the units we use, we observe that it is sufficient to make the order of 15 iterations with a

214 time step of 10 myrs corresponding to 150 myrs in total in order to reach a steady state.

215 In order to compute the heat transport field $\vec{u}$, we consider zero velocity in the continental crust

216 and we impose a rigid and constant movement along the parallel shape lines of the incoming plate.

217 We model the fluxes produced in the mantle wedge using a divergence free Stokes flux,

218 considering both momentum and mass conservation:

$$-\nu_A \, \Delta \vec{u} + \nabla p = 0 \qquad (3)$$

$$\nabla \cdot \vec{u} = 0 \qquad (4)$$

219 in the region Ω_A occupied by the mantle wedge, where $\vec{u} = (u_x, u_y)$ and p are the velocity and

220 pressure of the fluid flow and ν_A is the kinematic viscosity of the asthenosphere in the wedge

221 mantle. Thus, only for the wedge mantle, the velocity field $\vec{u} = (u_x, u_y)$ is computed from the

222   Stokes's variational formulation using finite elements of type P1b for the velocity (space U_h) and

223   P1 for the pressure (space P_h) by solving:

$$\nu_A \int_{\Omega_A} \frac{\partial u_x}{\partial x}\frac{\partial v_x}{\partial x} + \frac{\partial u_x}{\partial y}\frac{\partial v_x}{\partial y} + \frac{\partial u_y}{\partial x}\frac{\partial v_y}{\partial x} + \frac{\partial u_y}{\partial y}\frac{\partial v_y}{\partial y}$$

$$+ \int_{\Omega_A} \frac{\partial p}{\partial x}v_x + \frac{\partial p}{\partial y}v_y + q\left(\frac{\partial u_x}{\partial x} + \frac{\partial u_y}{\partial y}\right) = 0 \;\; \forall \vec{v} \in U_h, q \in P_h. \tag{5}$$

224   ### 4.1.2   Thermal Model Description (Boundary Conditions)

225   For the heat equation, we consider that the temperature on the edge condition of the

226   incoming/subducting plate increases in deep y by:

$$T(y) = T_S + (T_m - T_S)\,\mathrm{erf}\left(\frac{y}{\sqrt{4\kappa t}}\right) \tag{6}$$

227   where T_S=0 and T_m=1350 °C are the surface and mantle temperatures, where erf is the Gaussian

228   error function, t is the age of the plate (50 myrs) and κ is the thermal diffusivity of the incoming

229   plate. This is a good approximation for deep temperature profiles for low aged plates that is the

230   case for the entire Chilean trench (see Stein & Stein, 1992; Vöelker et al., 2011). For the other

231   boundary conditions (Figure 4), we assume that T varies quadratically from 1350° to 1400 °C in

232   interior of the right boundary of the mantle wedge, T=0 at the surface, T=1350 °C at the bottom

233   part of the subducting lithosphere and zero heat flux in the rest of the boundaries.

234   For the Stokes's equation, we take $\vec{u} = 0$ in the continental crust and $\vec{u} = u_0\vec{\tau}(y)$ in the subducting

235   lithosphere where u_0=67 mm/yr is the imposed constant speed of the incoming plate with $\vec{\tau}(y)$ the

236   unit tangent vector to the subducting lithosphere shape lines depending on depth y. The boundary

237   conditions for the flow in the mantle wedge are $\vec{u} = 0$ on the upper part of the wedge, $\vec{u} = u_0\vec{\tau}(y)$

238   on the lower part of the wedge and free flow in the right edge of the wedge. See Text S1 in the

239   supplementary information for more details.

4.1.2 Thermal Model Description (Parameter Selection)

241   Topography and bathymetry are taken from published data (Ryan et al., 2009). The geometry of

242   the subducted lithosphere is taken from Slab2.0 (Hayes et al., 2018). In addition, to assess our

243   model, we consider three different upper continental mantle depths of 60, 80 and 100 km.

244   However, as they show roughly similar results for the location of the mainshocks, we consider the

245   more realistic model of 60 km (Wada and Wang, 2009). Figures S16 and S17 show models with

246   80 and 100 km, respectively). A detail list of the other parameters used to develop the two-

247   dimensional model through finite element are listed in Table S5 where values are taken from

248   several authors (Hyndman & Wang, 1993; Herzberg et al., 2007; Wang et al., 1995; Oleskevich et

249   al., 1999; Vöelker et al., 2011, Höink et al., 2011) for rheologic and geometric values. Please note

250   that heat diffusivity takes different values in three different regions: the subduction lithosphere,

251   the upper part of the continental crust and sediments and the rest of the domain. For the sources of

252   temperature, we also consider different radiative sources in the upper and lower continental crust

253   and sediments.

4.2 Thermal Conditions of the Slab

255   From our results of the slab thermal-conditions in northern Chile (Figure 3d), we observe that E1

256   and its aftershocks occurs near the 400 ºC isotherm-depth and does not exceed the 450 ºC

257   isotherm, while the rest of the events occurs around or below this isotherm. Figures 3b and 3c

258   illustrate the relationship between the temperature of the slab at which events occur, the distance

259   from the top of the slab and number of aftershocks, respectively. Our analysis clearly reveals an

260   inverse relationship between the number of aftershocks and temperature. It is important to

261 highlight that E6, the deepest within the slab, occurs at the highest temperatures range between

262 700 – 800 ºC, and is the only event that does not exhibit aftershocks.

263

5 Seismic Source properties

5.1 Seismic Source Kinematic Inversions

266 Having observed a clear difference of aftershock productivity as function of depth, we now

267 attempt to resolve any difference in rupture properties. To obtain the slip distribution of each

268 mainshock, we perform kinematic inversions using near-field stations on hard rock (Leyton et

269 al., 2018) (Figure 1), including 19 strong-motion stations and one broad-band station (Figure

270 S17). Since it is not possible to distinguish the causative fault plane from aftershocks geometry,

271 we consider the two possible fault planes, according to moment tensors reported by the USGS

272 (Tables S3 and S4). We assume a finite-fault model with an a-priori elliptical-patch slip

273 distribution. This methodology has been successfully used by several authors (Madariaga and

274 Ruiz, 2016; Ruiz et al., 2019). We inverted seven parameters. Five of them, correspond to

275 geometrical characteristic: semi-axes a and b of the ellipse, the rotation angle of the ellipse α

276 and the location (x_0, y_0) of its center into the fault plane, and the other two parameters are

277 maximum slip D_{max} and rupture velocity V_r. From this inverted rupture model, we compute

278 dynamic parameters using circular crack approximation obtained averaging both axes of the

279 ellipse (Ruiz et al., 2019 and references there in). Strong motion and broad band records were

280 corrected for the instrumental response and linear trend, filtered using a causal Butterworth filter

281 with corner frequencies of 0.02 and 0.1 Hz, and then integrated to displacement. It is important

282 to mention that the high corner frequency is controlled by our simple elliptical model and the 1-

283 D velocity model (Husen et al., 1999) used to simulate the wave propagation from the source to

284 the receivers. The misfit between observed and synthetic records was computed using a L2 norm

285 starting from origin time up to 75 s later to avoid including surface waves, and considering both

286 possible rupture planes reported by the USGS (Tables S3 and S4).

5.2 Kinematic Parameters

288 Considering all six events, our results show similar geometries of rupture (Table 1), with an

289 approximately circular rupture ranging from ~3.5 to ~5 km.

290 Figure 5 shows an example of the kinematic inversion results, for event E1 considering NP1. The

291 observed and synthetic displacement waveforms show a good agreement, with a maximum value

292 about 0.4 cm for the East-West component in station A20P (waveforms for all events in

293 Supplementary Figures S1-S12). In addition, although there are differences in the misfit values

294 for each of the fault planes considered (Tables S3 and S4), these are small enough to give

295 preference to one or the other.

296 The estimated stress drop values vary between 7.5 MPa and 29.5 MPa (Table 1), which are high

297 compared with typical values for shallow earthquakes (Derode & Campos, 2019), but similar to

298 others observed for IDEs in Chile (Ruiz & Madariaga, 2011; Ruiz et al., 2019) and at global

299 scale (Poli & Prieto, 2014; Prieto et al., 2012). Despite a variability of rupture parameters exists

300 (Table 1), we do not see any clear correlation between them and the depth of the events. We thus

301   suggest that the analyzed events, while occurring under different thermal conditions, all have a

302   similar rupture physics.

303

304   **6 Discussion**

305   While co-seismic rupture properties do not vary with distance from the top of the slab, we

306   observe clear differences in the post-seismic activity pattern, with a decrease of the aftershocks

307   as the distance from the top of the slab and temperature increase (700-800 ºC isotherm-depths).

308   Difference in the number of aftershocks between E1 and the rest of events could be related to the

309   hypocenter-depth within the slab. E1 is located ~7 km from top of slab, close to the oceanic

310   Moho (Figure 1b; Patzwahl et al., 1999; Ranero and Sallarès, 2004). In addition, E1 aftershocks

311   locations reported by the CSN delineate a potential pre-existing fault aligned and similar to those

312   extensional faults located in the outer-rise region (Figure S13). These tensional faults are likely

313   caused by plate bending, and could provide a pathway for fluid infiltration, producing hydration

314   into the crust and uppermost mantle (Boneh et al., 2019; Contreras-Reyes et al., 2008; Iyer et al.,

315   2012). However, how deeply water can infiltrate is still under debate, since the buoyancy of

316   water (or equivalently, confining pressure) makes it difficult to bring water down even when

317   faulting is deep (Korenaga, 2017). By contrast, numeric models suggest that stress variation

318   induced by plate bending can produce sub-hydrostatic or even negative pressure gradients along

319   normal faults, favoring thus downward pumping of fluids (Faccenda et al., 2009). On the other

320   hand, previous studies in the DSZ of this region (Dorbath et al., 2008) observed that the upper

321   seismicity plane (USP) corresponding to oceanic crust, is characterized by intermediate V_p (~7.7

322   km/s) and low V_p/V_s (1.67) values, concluding that the USP is related to fluid releases associated

323 with metamorphic reactions occurring within jadeite-lawsonite blueschists. Similarly, it has been

324 observed that the USP has significantly larger b-values than the LSP (Florez & Prieto, 2019),

325 suggesting an hydrated USP and a relatively dry lithospheric mantle, since previous observations

326 have shown that high b-values anomalies correlate well with regions where dehydration reactions

327 are expected (Wiemer & Benoit, 1996) or with hydrated fracture zones (Schlaphorst et al., 2016).

328 Thus, this hydrated zone could lead to a greater occurrence of aftershocks.

329 Furthermore, we observe a dominant tensional stress regime, where mainshocks with normal

330 focal mechanism occur up to ~40 km from the top of the slab (i.e., 700 – 800 ºC isotherm). This

331 isotherm-depth interval is much deeper than the expected depth for this type of focal mechanism

332 compared to neutral plane of the stress field estimated by Seno & Yamanaka, (1996), who show

333 that the transition from tensional to compressional of outer rise events occur at the 400º-450 ºC

334 isotherm-depth. If this is correct, our results show that the plate bending becomes stronger during

335 subduction and is likely more predominant than the cyclic stresses associated to the seismic

336 coupling at the thrust zone at depths where IDEs occur (Seno & Yamanaka, 1996). Furthermore,

337 seismic tomographic studies off south-central Chile (Contreras-Reyes et al., 2008) and off

338 Nicaragua (Lefeldt et al., 2009) show a reduction in the upper oceanic mantle velocities from the

339 oceanic Moho up to 400º-450 ºC isotherm-depth. This lower bound has been interpreted as the

340 maximum potential depth for hydro-alteration within the upper part of the oceanic lithosphere,

341 where extensional stresses dominate, and fluids may not be able to penetrate any deeper than

342 neutral plane (Contreras-Reyes et al., 2008; Lefeldt et al., 2009; Faccenda et al., 2009). Another

343 proposed interpretation is that these seismic velocity anomalies could be related to small-crack

344 porosities, which can be produced by a mixture between thermal cracking and bending-related

345 faulting (Korenaga, 2017). As described above, our observations could suggest the existence of a

346 deepening of the neutral plane from 400-450 ºC to 700-800 ºC isotherm-depths regardless of the

347 presence of deep-water percolation.

348 A remaining question is, what could be controlling this deepening of the neutral plane along-dip?

349 Northern Chile corresponds to the region where the oceanic Nazca plate is relatively old (Figure

350 1) and therefore colder and with a deep fragile-ductile system (Figure 6), with an age of 54 Ma

351 near the trench axis (Müller et al., 2008) and 58 Ma estimated for the area where the mainshocks

352 occur. A plausible mechanism for a deepening of the neutral plane along-dip in northern Chile

353 would be the increase in bending stresses due to a greater slab-pull associated to the relative old,

354 cold and heavier already subducted oceanic Nazca plate. In particular, in this segment of the

355 Chilean margin, the largest known IDE has been registered for the slab-pull Tarapacá 2005 Mw

356 7.7 event (Peyrat et al., 2006; Legrand and Delouis, 2006; Kuge et al., 2010; Ruiz and

357 Madariaga, 2018). Moreover, the 1950 Ms 8.0 tensional event (Kausel & Campos, 1992)

358 occurred a little further south, reflecting the tensional character of the stress field within the

359 subducting slab. We also note how the moment tensors in northern Chile DSZ show a downdip

360 extensive stress field throughout the seismically active area (Sippl et al., 2019), which may imply

361 that plate bending, and unbending forces are small compared to slab-pull forces. Another

362 mechanism previously proposed by Kita et al. (2010) to explain the difference in the location of

363 the neutral plane beneath Tohoku and Hokkaido in the northeastern Japan is related to

364 differences in the thermal structure between the two regions. They concluded that the thermal

365 age of the subducted lithosphere and the oblique component of convergence rate affect the

366 density of the mantle wedge. This process triggers buoyancy force variations exerted in the slab

367 affecting finally the stress field of the subducting slab. However, this mechanism should be more

368   dominant along strike (thermal variations are more important in that direction) rather than in

369   along dip.

370   On the other hand, the occurrence of tensional events up to depths of 40 km as E6 is consistent

371   with the brittle region predicted by a yield strength envelope (YSE) for an oceanic lithosphere

372   under tensional stresses (Figure 6), which reaches depths of 40-42 km for olivine and dry olivine

373   mineralogy, and it decreases for wet conditions. Likewise, using high-precision relocations, a

374   DSZ south of Iquique (21.5 °S) is observed (Rietbrock & Waldhauser, 2004), with

375   predominantly extensional faulting in both seismic layers, and a clear down-dip tensional regime

376   with T-axes oriented in slab-parallel directions (Rietbrock & Waldhauser, 2004; Sippl et al.,

377   2019). The consistency between the strength envelope and the maximum depths of intraplate

378   tensional events suggests that these earthquakes have ruptured through the entire brittle part of

379   the oceanic lithosphere. Another interesting observation is that events E5 and E6 highlight for its

380   isotherm-depth occurrence, about 700-800 °C, which are higher than the stability limit of

381   antigorite at 600–650 °C commonly proposed as a lower limit for the LSP. As observed by Sippl

382   et al. (2018; 2019) these events are more common in the Northern Chile DSZ, and a runaway-

383   type process could be responsible, under specific conditions in the lower plate (e.g. composition,

384   hydration, stress state). Likewise, according to McKenzie et al. (2005) particularly large strain

385   rates could also lead to earthquakes in regions below the 600–650 °C isotherm-depth. In our

386   study region, this could be related to an increase in the slab pull. Finally, thermal cracking

387   hypothesis (Korenaga, 2017) could also play a role, since the deepest hydrated cracks could be

388   more widely spaced than the most superficial cracks

389   Considering previous observations and our own results, we propose a conceptual model shown in

390   Figure 7, where the processes that occur are as follows: (1) in the outer-rise region extensional

391   bend-faulting occur and lead to partial hydration of the crust and upper mantle. However, fluids

392   may not be able to penetrate any deeper than neutral plane (approximately 450 ºC isotherm-

393   depth). Thus, the neutral plane separates a high-hydrated from a dry or poorly hydrated zones.

394   (2) As the oceanic plate subducts, a deepening of the neutral plane occurs by the increase of the

395   slab-pull forces, separating it from the 450 ºC isotherm, and increasing the region subject to

396   extensional failure. (3) Normal (tensional) events occur at different distances from the top of the

397   slab, but their behavior is mostly controlled by variable physical background conditions. In

398   particular, in the high-hydrated region a greater number of aftershocks is observed, differently

399   from what is observed in the dry deeper zone.

400

401   **7 Conclusions**

402   We presented a detailed study of seismic source and aftershock productivity for the six largest

403   IDEs occurred in northern in Chile since 2010 and recorded by dense seismic arrays in the near-

404   field. Our results show that, although all of these events are located at different depths and under

405   different thermal conditions, all have similar rupture physics, with analogous geometries

406   considering an elliptical-patch approach and stress drop values between 7 MPa and 30 MPa. On

407   the other hand, a clear decrease of the number of aftershocks as the distance from the top of the

408   slab and temperature increase is observed. We propose that this behavior could be controlled by

409   the incoming plate hydration, where the 400 – 450 ºC isotherm-depths and neutral plane of the

410   stress field acts as limits for hydration in the outer-rise region, which is deepened by the slab-pull

411   as the slab subducts.

412

Declaration of competing interest

The authors declare that they have no known competing financial interests or personal relationships that could have appeared to influence the work reported in this paper.

References

Barrientos, S., & National Seismological Center (CSN) Team. (2018). The seismic network of Chile. *Seismological Research Letters*, 89(2A), 467-474.

Beck, S. L., Zandt, G., & Wagner, L. (2010). Central Andean uplift and the geodynamics of the high topography. Other/Seismic Network, International Federation of Digital Seismograph Networks.

Boneh, Y., Schottenfels, E., Kwong, K., van Zelst, I., Tong, X., Eimer, M., Miller, M., Moresi, L., Warren, J., Wiens, D., Billen, M., Naliboff, J., & Zhan, Z. (2019). Intermediate-depth earthquakes controlled by incoming plate hydration along bending-related faults. *Geophysical Research Letters*, 46(7), 3688-3697.

Comte, D., Dorbath, L., Pardo, M., Monfret, T., Haessler, H., Rivera, L., Frogneux, M., Glass, B., & Meneses, C. (1999). A double-layered seismic zone in Arica, northern Chile. *Geophysical Research Letters*, 26(13), 1965-1968.

Contreras-Reyes, E., Grevemeyer, I., Flueh, E. R., & Reichert, C. (2008). Upper lithospheric structure of the subduction zone offshore of southern Arauco peninsula, Chile, at~ 38 S. *Journal of Geophysical Research: Solid Earth*, 113(B7).

Contreras-Reyes, E., & Osses, A. (2010). Lithospheric flexure modelling seaward of the Chile trench: implications for oceanic plate weakening in the Trench Outer Rise region. *Geophysical Journal International*, 182(1), 97-112.

Contreras-Reyes, E, J. Jara, I. Grevemeyer, S. Ruiz, and D. Carrizo (2012). Abrupt change in the dip of the subducting plate beneath north Chile. *Nature Geoscience, 5, 342-345*.

453   Contreras-Reyes, E. (2018). Structure and tectonics of the Chilean convergent margin from

454   wide-angle seismic studies: a review. In The Evolution of the Chilean-Argentinean Andes (pp. 3-

455   29). Springer, Cham.

456   Dascher-Cousineau, K., Brodsky, E., Lay, T., & Goebel, T. (2020). What controls variations in

457   aftershock productivity?. *Geophysical Research Letters*.

458   Delouis, B., & Legrand, D. (2007). Mw 7.8 Tarapaca intermediate depth earthquake of 13 June

459   2005 (northern Chile): Fault plane identification and slip distribution by waveform inversion.

460   Geophysical Research Letters, 34(1).

461   DeMets, C., Gordon, R. G., & Argus, D. F. (2010). Geologically current plate motions.

462   *Geophysical Journal International*, 181(1), 1-80.

463   Derode, B., & Campos, J. (2019). Energy Budget of Intermediate-Depth Earthquakes in Northern

464   Chile: Comparison With Shallow Earthquakes and Implications of Rupture Velocity Models

465   Used. *Geophysical Research Letters*, 46(5), 2484-2493.

466   Dorbath, C., Gerbault, M., Carlier, G., & Guiraud, M. (2008). Double seismic zone of the Nazca

467   plate in northern Chile: High-resolution velocity structure, petrological implications, and

468   thermomechanical modeling. *Geochemistry, Geophysics, Geosystems*, 9(7).

469   Ferrand, T. P., Hilairet, N., Incel, S., Deldicque, D., Labrousse, L., Gasc, J., Renner, J., Wang,

470   Y., Green, H., & Schubnel, A. (2017). Dehydration-driven stress transfer triggers intermediate-

471   depth earthquakes. *Nature communications*, 8(1), 1-11.

472   Frank, W. B., Poli, P., & Perfettini, H. (2017). Mapping the rheology of the Central Chile

473   subduction zone with aftershocks. *Geophysical Research Letters*, 44(11), 5374-5382.

474 Florez, M. A., & Prieto, G. A. (2019). Controlling factors of seismicity and geometry in double

475 seismic zones. *Geophysical Research Letters*, 46(8), 4174-4181.

476 Frohlich, C. (1987). Aftershocks and temporal clustering of deep earthquakes. *Journal of*

477 *Geophysical Research: Solid Earth*, 92(B13), 13944-13956.

478 Frohlich, C. (2006). Deep earthquakes. Cambridge university press.

479 Geersen, J., Ranero, C. R., Klaucke, I., Behrmann, J. H., Kopp, H., Tréhu, A. M., Contreras-

480 Reyes, E., Barckhausen, U. & Reichert, C. (2018). Active tectonics of the North Chilean marine

481 forearc and adjacent oceanic Nazca Plate. *Tectonics*, 37(11), 4194-4211.

482 GFZ German Research Centre for Geosciences; Institut des Sciences de l'Univers-Centre

483 National de la Recherche CNRS-INSU (2006): IPOC Seismic Network. Integrated Plate

484 boundary Observatory Chile - IPOC. Other/Seismic Network. doi.org/10.14470/PK615318.

485 Goetze, C. (1978). The mechanisms of creep in olivine. *Philosophical Transactions of the Royal*

486 *Society of London. Series A, Mathematical and Physical Sciences*, 288(1350), 99-119.

487 Hacker, B. R., Peacock, S. M., Abers, G. A., & Holloway, S. D. (2003). Subduction factory 2.

488 Are intermediate-depth earthquakes in subducting slabs linked to metamorphic dehydration

489 reactions?. *Journal of Geophysical Research: Solid Earth*, 108(B1).

490 Hainzl, S., Sippl, C., & Schurr, B. (2019). Linear relationship between aftershock productivity

491 and seismic coupling in the Northern Chile subduction zone. *Journal of Geophysical Research:*

492 *Solid Earth*, 124(8), 8726-8738.

493 Hayes, G. P., Moore, G. L., Portner, D. E., Hearne, M., Flamme, H., Furtney, M., & Smoczyk,

494 G. M. (2018). Slab2, a comprehensive subduction zone geometry model. *Science*, 362(6410), 58-

495 61.

496 Herzberg, C., Asimow, P. D., Arndt, N., Niu, Y., Lesher, C. M., Fitton, J. G., ... & Saunders, A.

497 D. (2007). Temperatures in ambient mantle and plumes: Constraints from basalts, picrites, and

498 komatiites. *Geochemistry, Geophysics, Geosystems*, 8(2).

499 Höink, T., Jellinek, A. M., and Lenardic, A. (2011), Viscous coupling at the lithosphere-

500 asthenosphere boundary, Geochem. Geophys. Geosyst., 12.

501 Houston, H. (2015). Deep earthquakes. Elsevier.

502 Husen, S., Kissling, E., Flueh, E., & Asch, G. (1999). Accurate hypocenter determination in the

503 shallow part of the Nazca subduction zone in Northern Chile using a combined on-/offshore

504 network. *Geophysical Journal International*, 138, 687-701.

505 Hyndman, R. D., & Wang, K. (1993). Thermal constraints on the zone of major thrust

506 earthquake failure: The Cascadia subduction zone. *Journal of Geophysical Research: Solid

507 Earth*, 98(B2), 2039-2060.

508 Iyer, K., Rüpke, L. H., Phipps Morgan, J., & Grevemeyer, I. (2012). Controls of faulting and

509 reaction kinetics on serpentinization and double Benioff zones. *Geochemistry, Geophysics,

510 Geosystems*, 13(9).

511 John, T., Medvedev, S., Rüpke, L. H., Andersen, T. B., Podladchikov, Y. Y., & Austrheim, H.

512 (2009). Generation of intermediate-depth earthquakes by self-localizing thermal runaway.

513 *Nature Geoscience*, 2(2), 137-140.

514 Jung, H., Green Ii, H. W., & Dobrzhinetskaya, L. F. (2004). Intermediate-depth earthquake

515 faulting by dehydration embrittlement with negative volume change. *Nature*, 428(6982), 545-

516 549.

517   Kausel, E., & Campos, J. (1992). The Ms= 8 tensional earthquake of 9 December 1950 of

518   northern Chile and its relation to the seismic potential of the region. *Physics of the earth and*

519   *planetary interiors*, 72(3-4), 220-235.

520   Karato, S. I., Paterson, M. S., & FitzGerald, J. D. (1986). Rheology of synthetic olivine

521   aggregates: influence of grain size and water. *Journal of Geophysical Research: Solid Earth*,

522   91(B8), 8151-8176.

523   Khazaradze, G., & Klotz, J. (2003). Short-and long-term effects of GPS measured crustal

524   deformation rates along the south central Andes. *Journal of Geophysical Research: Solid Earth*,

525   108(B6).

526   Kirby, S. H., Durham, W. B., & Stern, L. A. (1991). Mantle phase changes and deep-earthquake

527   faulting in subducting lithosphere. *Science*, 252(5003), 216-225.

528   Kirby, S. (1995). Interslab earthquakes and phase changes in subducting lithosphere. *Reviews of*

529   *Geophysics*, 33(S1), 287-297.

530   Kita, S., Okada, T., Hasegawa, A., Nakajima, J., & Matsuzawa, T. (2010). Existence of

531   interplane earthquakes and neutral stress boundary between the upper and lower planes of the

532   double seismic zone beneath Tohoku and Hokkaido, northeastern Japan. *Tectonophysics*, 496(1-

533   4), 68-82.

534   Kohlstedt, D. L., Evans, B., & Mackwell, S. J. (1995). Strength of the lithosphere: Constraints

535   imposed by laboratory experiments. *Journal of Geophysical Research: Solid Earth*, 100(B9),

536   17587-17602.

537   Korenaga, J. (2017). On the extent of mantle hydration caused by plate bending. *Earth and*

538   *Planetary Science Letters*, 457, 1-9.

539   Kuge, K., Kase, Y., Urata, Y., Campos, J., & Perez, A. (2010). Rupture characteristics of the

540   2005 Tarapaca, northern Chile, intermediate-depth earthquake: Evidence for heterogeneous fluid

541   distribution across the subducting oceanic plate?. Journal of Geophysical Research: Solid Earth,

542   115(B9).

543   Kukowski, N., & Oncken, O. (2006). Subduction erosion—The "normal" mode of fore-arc

544   material transfer along the Chilean margin?. In The Andes (pp. 217-236). Springer, Berlin,

545   Heidelberg.

546   Leyton, F., Leopold, A., Hurtado, G., Pastén, C., Ruiz, S., Montalva, G., & Saez, E. (2018).

547   Geophysical characterization of the Chilean seismological stations: First results. *Seismological*

548   *Research Letters*, 89(2A), 519-525.

549   Lefeldt, M., Grevemeyer, I., Goßler, J., & Bialas, J. (2009). Intraplate seismicity and related

550   mantle hydration at the Nicaraguan trench outer rise. *Geophysical Journal International*, 178(2),

551   742-752.

552   Li, C., Peng, Z., Yao, D., Guo, H., Zhan, Z., & Zhang, H. (2018). Abundant aftershock sequence

553   of the 2015 M w7. 5 Hindu Kush intermediate-depth earthquake. *Geophysical Journal*

554   *International*, 213(2), 1121-1134.

555   Madariaga, R., and S. Ruiz (2016). Earthquake dynamics on circular faults: A review 1970–

556   2015, J. Seismol. 20, 1235–1252, doi: 10.1007/s10950-016-9590-8.

557   Maksymowicz, A., & Tassara, A. (2018). The Geometry of the Continental Wedge and Its

558   Relation to the Rheology and Seismicity of the Chilean Interplate Boundary. In The Evolution of

559   the Chilean-Argentinean Andes (pp. 31-58). Springer, Cham.

560 McKenzie, D., Jackson, J., & Priestley, K. (2005). Thermal structure of oceanic and continental

561 lithosphere. *Earth and Planetary Science Letters*, 233(3-4), 337-349.

562 Müller, R. D., Sdrolias, M., Gaina, C., & Roest, W. R. (2008). Age, spreading rates, and

563 spreading asymmetry of the world's ocean crust. *Geochemistry, Geophysics, Geosystems*, 9(4).

564 Ohuchi, T., Lei, X., Ohfuji, H., Higo, Y., Tange, Y., Sakai, T., Fujino, K., & Irifune, T. (2017).

565 Intermediate-depth earthquakes linked to localized heating in dunite and harzburgite. *Nature

566 Geoscience*, 10(10), 771-776.

567 Oleskevich, D. A., Hyndman, R. D., & Wang, K. (1999). The updip and downdip limits to great

568 subduction earthquakes: Thermal and structural models of Cascadia, south Alaska, SW Japan,

569 and Chile. *Journal of Geophysical Research: Solid Earth*, 104(B7), 14965-14991.

570 Patzwahl, R., Mechie, J., Schulze, A., & Giese, P. (1999). Two-dimensional velocity models of

571 the Nazca plate subduction zone between 19.5° S and 25° S from wide-angle seismic

572 measurements during the CINCA95 project. *Journal of Geophysical Research: Solid Earth*,

573 104(B4), 7293-7317.

574 Peacock, S. M. (2001). Are the lower planes of double seismic zones caused by serpentine

575 dehydration in subducting oceanic mantle?. *Geology*, 29(4), 299-302.

576 Peng, Z., & Zhao, P. (2009). Migration of early aftershocks following the 2004 Parkfield

577 earthquake. *Nature Geoscience*, 2(12), 877-881.

578 Persh, S. E., & Houston, H. (2004). Strongly depth-dependent aftershock production in deep

579 earthquakes. *Bulletin of the Seismological Society of America*, 94(5), 1808-1816.

580 Peyrat, S., Campos, J., De Chabalier, J. B., Perez, A., Bonvalot, S., Bouin, M. P., Legrand, D.,

581 Nercessian, A., Charade, O., Patau, G., Clévédé, E., Kausel, E., Bernard, P. & Vilotte, J.-P.

582   (2006). Tarapacá intermediate-depth earthquake (Mw 7.7, 2005, northern Chile): A slab-pull

583   event with horizontal fault plane constrained from seismologic and geodetic observations.

584   *Geophysical Research Letters*, 33(22).

585   Poli, P., & Prieto, G. (2014). Global and along-strike variations of source duration and scaling

586   for intermediate-depth and deep-focus earthquakes. *Geophysical Research Letters*, 41(23), 8315-

587   8324.

588   Poli, P., Prieto, G., Rivera, E., & Ruiz, S. (2016). Earthquakes initiation and thermal shear

589   instability in the Hindu Kush intermediate depth nest. *Geophysical Research Letters*, 43(4),

590   1537-1542.

591   Prieto, G. A., Beroza, G. C., Barrett, S. A., López, G. A., & Florez, M. (2012). Earthquake nests

592   as natural laboratories for the study of intermediate-depth earthquake mechanics.

593   *Tectonophysics*, 570, 42-56.

594   Ranero, C. R., & Sallarès, V. (2004). Geophysical evidence for hydration of the crust and mantle

595   of the Nazca plate during bending at the north Chile trench. *Geology*, 32(7), 549-552.

596   Ranero, C. R., Villaseñor, A., Phipps Morgan, J., & Weinrebe, W. (2005). Relationship between

597   bend-faulting at trenches and intermediate-depth seismicity. *Geochemistry, Geophysics,*

598   *Geosystems*, 6(12).

599   Reynard, B., Nakajima, J., & Kawakatsu, H. (2010). Earthquakes and plastic deformation of

600   anhydrous slab mantle in double Wadati-Benioff zones. *Geophysical Research Letters,* 37(24).

601   Richardson, E., & Jordan, T. H. (2002). Low-frequency properties of intermediate-focus

602   earthquakes. *Bulletin of the Seismological Society of America*, 92(6), 2434-2448.

603   Rietbrock, A., & Waldhauser, F. (2004). A narrowly spaced double-seismic zone in the

604   subducting Nazca plate. *Geophysical Research Letters*, 31(10).

605   Ruiz, S., & Madariaga, R. (2011). Determination of the friction law parameters of the Mw 6.7

606   Michilla earthquake in northern Chile by dynamic inversion. *Geophysical Research Letters*,

607   38(9).

608   Ruiz, S., and R. Madariaga. "Historical and recent large megathrust earthquakes in Chile."

609   Tectonophysics 733 (2018): 37-56.

610   Ruiz, S., Ammirati, J. B., Leyton, F., Cabrera, L., Potin, B., & Madariaga, R. (2019). The

611   January 2019 (M w 6.7) Coquimbo Earthquake: Insights from a Seismic Sequence within the

612   Nazca Plate. Seismological Research Letters, 90(5), 1836-1843.

613   Rutland, R. W. R. (1971). Andean orogeny and ocean floor spreading. *Nature*, 233(5317), 252-

614   255.

615   Ryan, W. B., Carbotte, S. M., Coplan, J. O., O'Hara, S., Melkonian, A., Arko, R., Weissel, R. A.,

616   Ferrini, V., Goodwillie, A., Nitsche, F., Bonczkowski, J. & Zemsky, R. (2009). Global multi-

617   resolution topography synthesis. *Geochemistry, Geophysics, Geosystems*, 10(3).

618   Schlaphorst, D., Kendall, J. M., Collier, J. S., Verdon, J. P., Blundy, J., Baptie, B., Latchman, J.,

619   Massin, F., & Bouin, M. P. (2016). Water, oceanic fracture zones and the lubrication of

620   subducting plate boundaries—insights from seismicity. *Geophysical Journal International,*

621   204(3), 1405-1420.

622   Seno, T., & Yamanaka, Y. (1996). Double seismic zones, compressional deep trench-outer rise

623   events, and superplumes. *Subduction: top to bottom,* 96, 347-355.

624 Senobari, N. S., Funning, G. J., Keogh, E., Zhu, Y., Yeh, C. C. M., Zimmerman, Z., & Mueen,

625 A. (2019). Super-Efficient Cross-Correlation (SEC-C): A Fast Matched Filtering Code Suitable

626 for Desktop Computers. *Seismological Research Letters*, 90(1), 322-334.

627 Shebalin, P., & Narteau, C. (2017). Depth dependent stress revealed by aftershocks. *Nature*

628 *communications*, 8(1), 1-8.

629 Shelly, D. R., Beroza, G. C., & Ide, S. (2007). Non-volcanic tremor and low-frequency

630 earthquake swarms. *Nature*, 446(7133), 305-307.

631 Sippl, C., Schurr, B., Asch, G., & Kummerow, J. (2018). Seismicity structure of the northern

632 Chile forearc from> 100,000 double-difference relocated hypocenters. *Journal of Geophysical*

633 *Research: Solid Earth*, 123(5), 4063-4087.

634 Sippl, C., Schurr, B., John, T., & Hainzl, S. (2019). Filling the gap in a double seismic zone:

635 Intraslab seismicity in Northern Chile. *Lithos*, 346, 105155.

636 Stern, C. R. (2011). Subduction erosion: rates, mechanisms, and its role in arc magmatism and

637 the evolution of the continental crust and mantle. *Gondwana Research*, 20(2-3), 284-308.

638 Stein, C. A., & Stein, S. (1992). A model for the global variation in oceanic depth and heat flow

639 with lithospheric age. Nature, 359(6391), 123-129.

640 Tassara, A., & Echaurren, A. (2012). Anatomy of the Andean subduction zone: three-

641 dimensional density model upgraded and compared against global-scale models. *Geophysical*

642 *Journal International*, 189(1), 161-168.

643 Völker, D., Grevemeyer, I., Stipp, M., Wang, K., & He, J. (2011). Thermal control of the

644 seismogenic zone of southern central Chile. *Journal of Geophysical Research: Solid Earth*,

645 116(B10).

646 Wada, I., & Wang, K. (2009). Common depth of slab-mantle decoupling: Reconciling diversity

647 and uniformity of subduction zones. *Geochemistry, Geophysics, Geosystems*, 10(10).

648 Wang, K., Hyndman, R. D., & Yamano, M. (1995). Thermal regime of the Southwest Japan

649 subduction zone: effects of age history of the subducting plate. Tectonophysics, 248(1-2), 53-69.

650 Wessel, P., Luis, J. F., Uieda, L., Scharroo, R., Wobbe, F., Smith, W. H. F., & Tian, D. (2019).

651 The generic mapping tools version 6. Geochemistry, Geophysics, Geosystems, 20(11), 5556-

652 5564.

653 Wiemer, S., & Benoit, J. P. (1996). Mapping the b-value anomaly at 100 km depth in the Alaska

654 and New Zealand subduction zones. *Geophysical Research Letters*, 23(13), 1557-1560.

655 Wiens, D. A., McGuire, J. J., Shore, P. J., Bevis, M. G., Draunidalo, K., Prasad, G., & Helu, S. P.

656 (1994). A deep earthquake aftershock sequence and implications for the rupture mechanism of

657 deep earthquakes. *Nature*, 372(6506), 540-543.

658 Wiens, D. A., & Gilbert, H. J. (1996). Effect of slab temperature on deep-earthquake aftershock

659 productivity and magnitude–frequency relations. *Nature*, 384(6605), 153-156.

660 Wiens, D. A. (2001). Seismological constraints on the mechanism of deep earthquakes:

661 Temperature dependence of deep earthquake source properties. *Physics of the Earth and*

662 *Planetary Interiors*, 127(1-4), 145-163.

663 Zhan, Z., Helmberger, D. V., Kanamori, H., & Shearer, P. M. (2014). Supershear rupture in a

664 Mw 6.7 aftershock of the 2013 Sea of Okhotsk earthquake. *Science*, 345(6193), 204-207.

665

666　**Table 1**

667　*Resume of kinematic parameters and number of aftershocks obtained for each mainshock.*

Event	a (km)	b (km)	D_{max} (m)	V_r (km/s)	Stress drop (MPa)	Number of aftershocks	Distance from the top of the slab (km)
E1	3.49	5.13	1.08	1.07	18.2	2044	7
	3.67	5.68	0.94	1.19	14.7		
E2	4.38	6.99	0.65	1.59	8.5	123	12
	4.12	6.58	0.73	1.51	9.9		
E3	5.05	6.16	1.12	0.67	14.3	30	14
	4.14	6.44	1.24	0.82	16.7		
E4	4.70	3.90	0.73	1.22	12.8	46	20
	4.56	5.60	0.52	1.91	7.5		
E5	5.89	4.25	0.71	1.68	10.0	16	38
	4.88	6.11	0.60	2.20	8.1		
E6	3.12	4.42	1.61	0.68	29.5	0	41
	3.43	6.40	0.95	0.80	14.1		

668　Note: Green and yellow rows indicate parameters obtained using nodal plane 1 (NP1) and nodal plane 2 (NP2). For more details
669　see Tables S3 and S4.

670
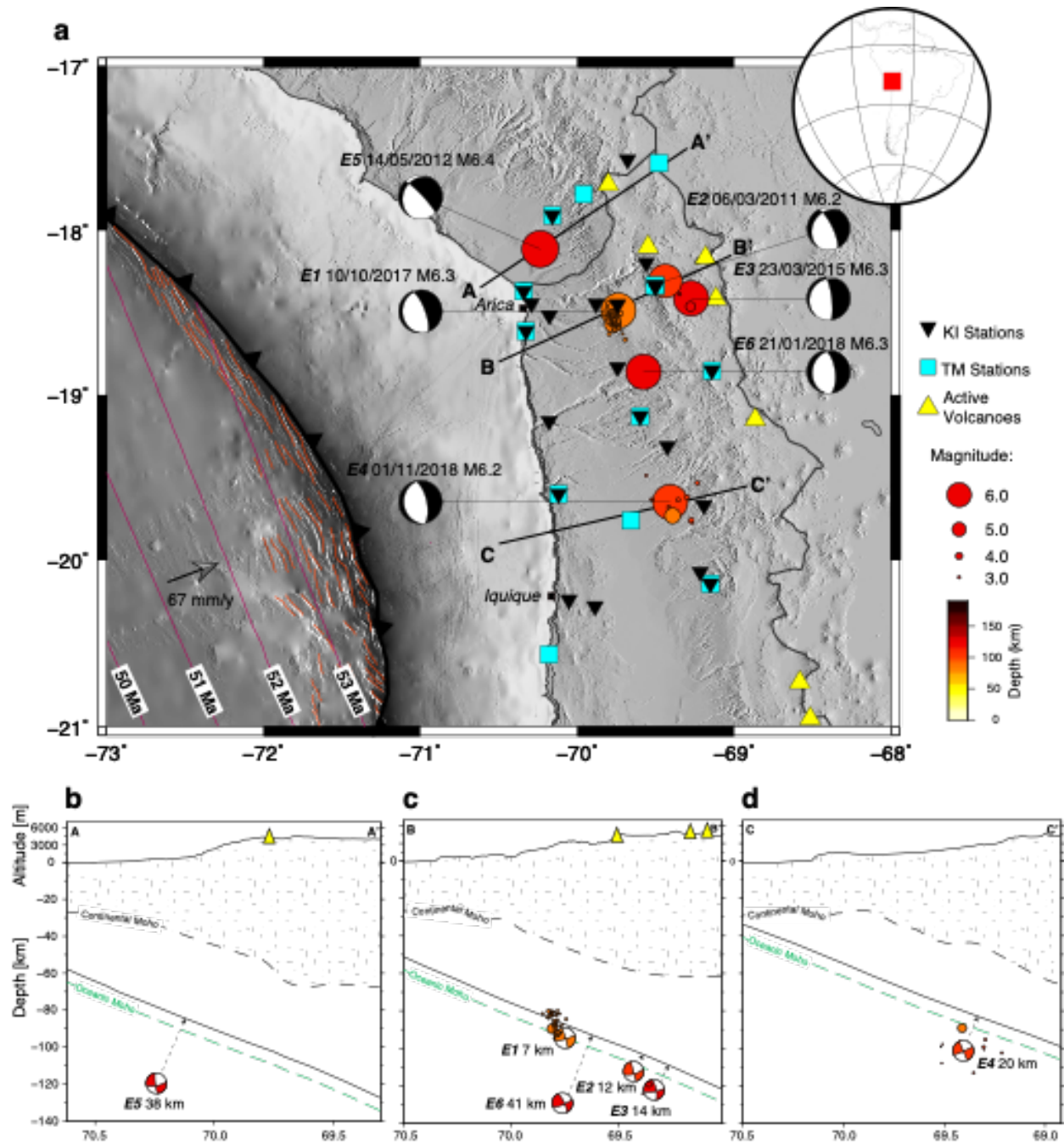
Figure 1. Seismotectonic setting of the northern Chile region. **a** Orange circles indicate the mainshocks (labeled as E1, E2 and so on according to their distance from the top of the slab) and aftershocks epicenters (CSN catalogue), scaled and colored by magnitude and depth. Focal mechanisms are obtained from USGS, and also date and magnitude according to CSN are indicated. Black inverted triangles and cyan squares are the locations of the stations used for the kinematic inversions (KI) and template matching (TM), respectively. Yellow triangles represent active volcanoes. Red lines indicate faulting located on the outer-rise region. Isochrones for the Nazca plate (Müller et al., 2008) are indicated with magenta lines. (Inset) Global map with the

678 specified study area. **b**, **c** and **d** cross sections along segments AA', BB' and CC' respectively in **a**. Distance from the top of the

679 slab is indicated for each mainshock. The slab (black solid line) corresponds to the projection along cross-sections of the Nazca

680 slab model SLAB2.0 (Hayes et al., 2018). Black and green dashed lines correspond to continental Moho (Tassara & Echaurren,

681 2012) and oceanic Moho (Contreras-Reyes et al., 2012), respectively.

682

683
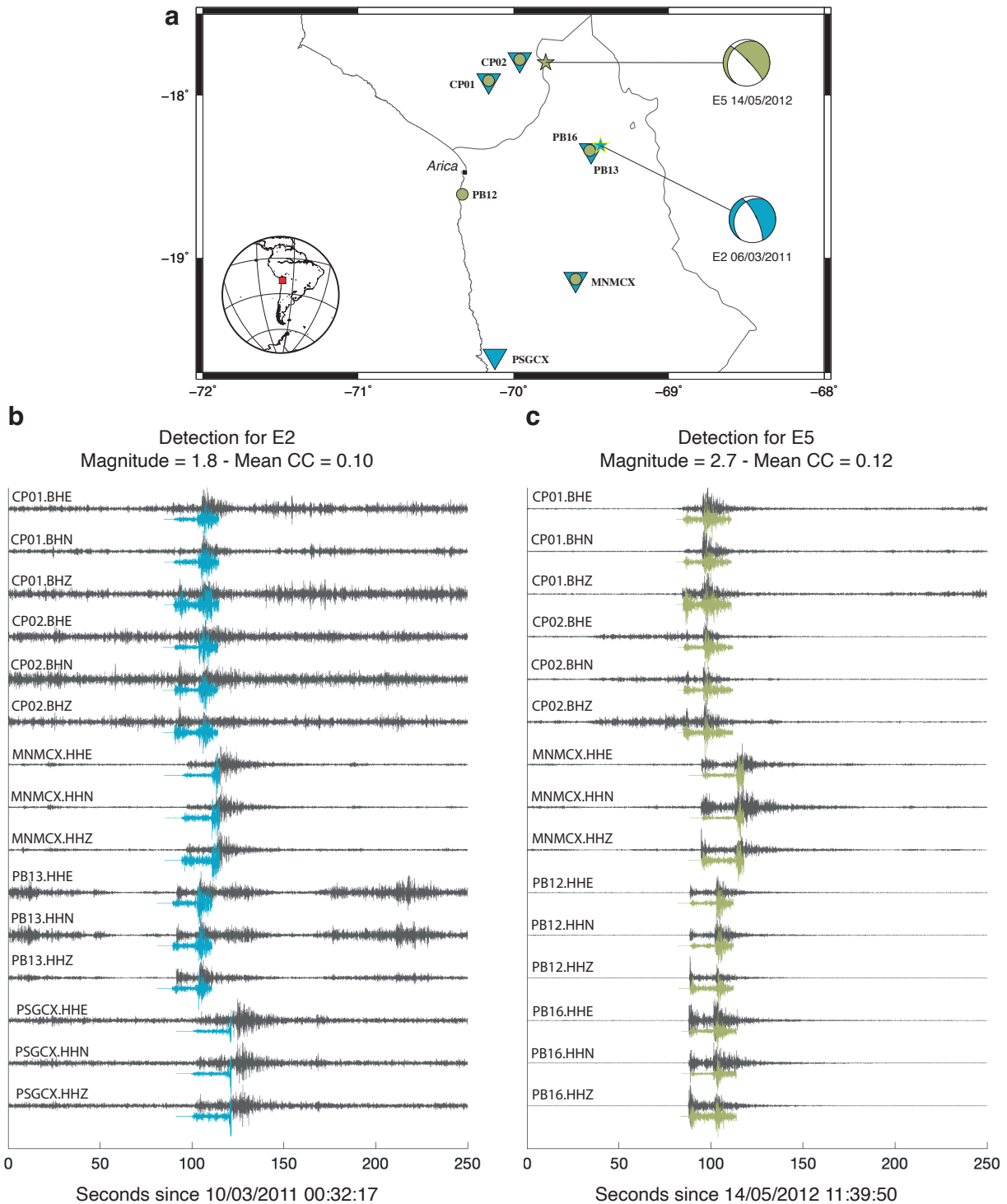
Figure 2. Example of new events detected using template matching. **a** Map of stations used for E2 (cyan inverted triangles) and E5 (green dots). Stars represent epicenter for each event (CSN), and their focal mechanism according to USGS are also plotted. (Inset) Global map with the specified study area. **b** Example of a new detection in the continuous data for E2. Cyan traces represent templates aligned considering their respective moveouts. The average correlation coefficient (Mean CC) is 0.10 and the inferred magnitude (Mw) 1.8. **c** Example of a new detection in the continuous data for E5. Green traces represent templates aligned considering their respective moveouts. The average correlation coefficient (Mean CC) is 0.12 and the inferred magnitude (Mw) for the new event is 2.7.

691
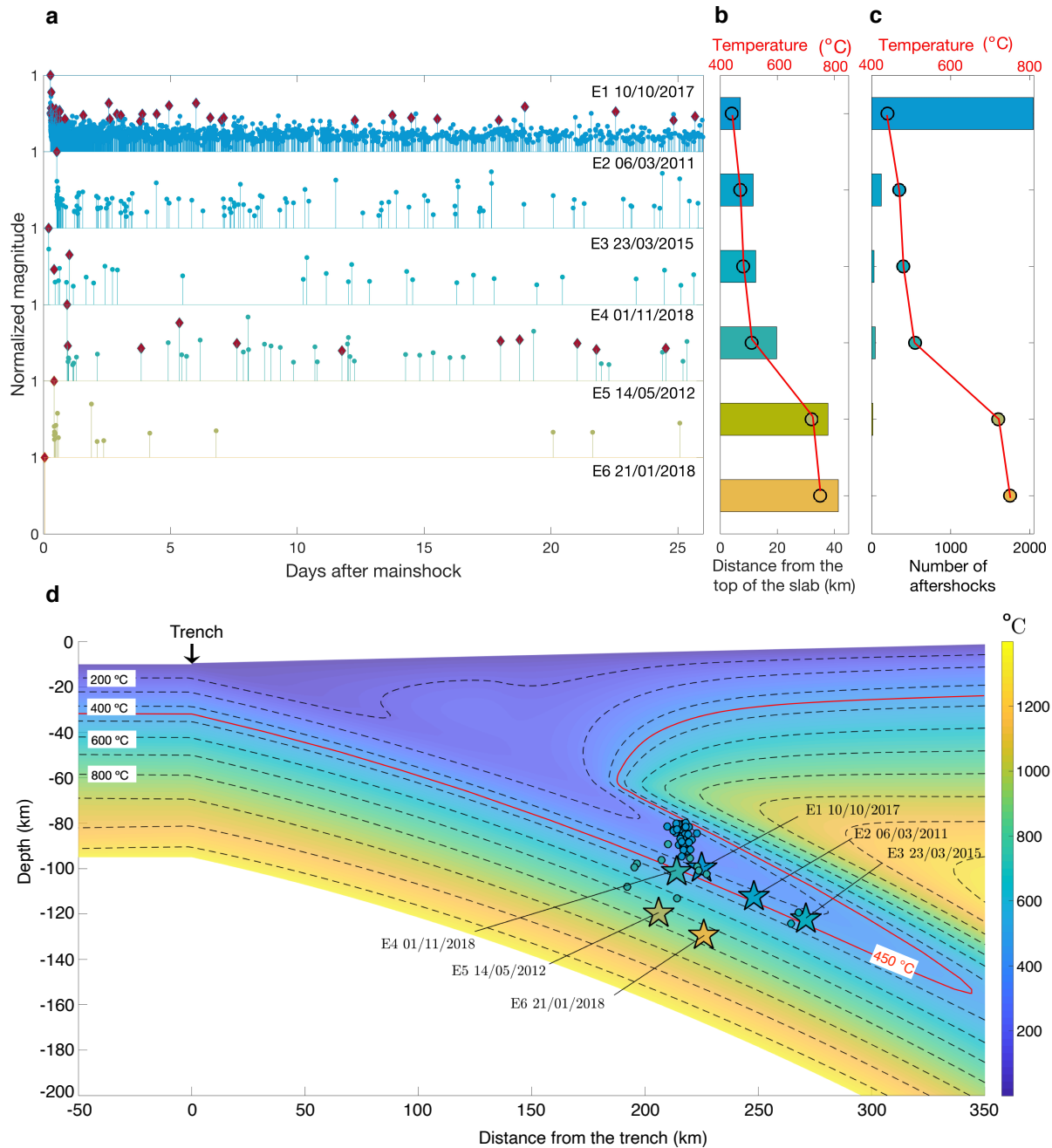
Figure 3. Results for aftershocks efficency and thermal model. **a** Detections using TM. For each row, stems show aftershocks detections until 25 days after mainshocks using TM as indicated in section 2.1. Stem height is normalized by the mainshock magnitude,and templates used are indicated as magenta diamonds. **b** Distance from the top of slab (Figure 1) is indicated with horizontal bars, and red line shows estimated temperature for hypocenter location according to the thermal model in **d**. **c** Horizontal bars indicate total number of aftershocks and red line the temperature. **d** Thermal model for northern Chile.

698   Mainshock hypocenters and its aftershocks reported by the CSN are indicated with stars and circles, respectively. In addition,

699   trench and dates of events are labeled.
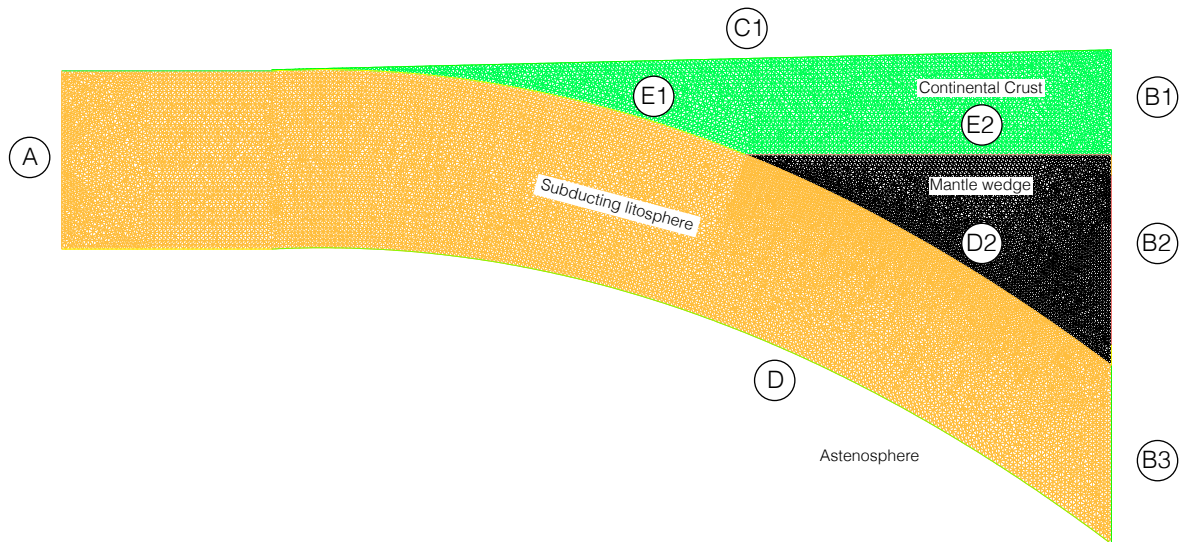
700

701   **Figure 4.** FEM grid and boundary conditions used for thermal numerical modelling. Continental crust, mantle wedge and oceanic
702   plate are indicated with green, black, and light brown colors, respectively. Capital letters circled represent where border conditions
703   are imposed (see details in Text S1).

704

705
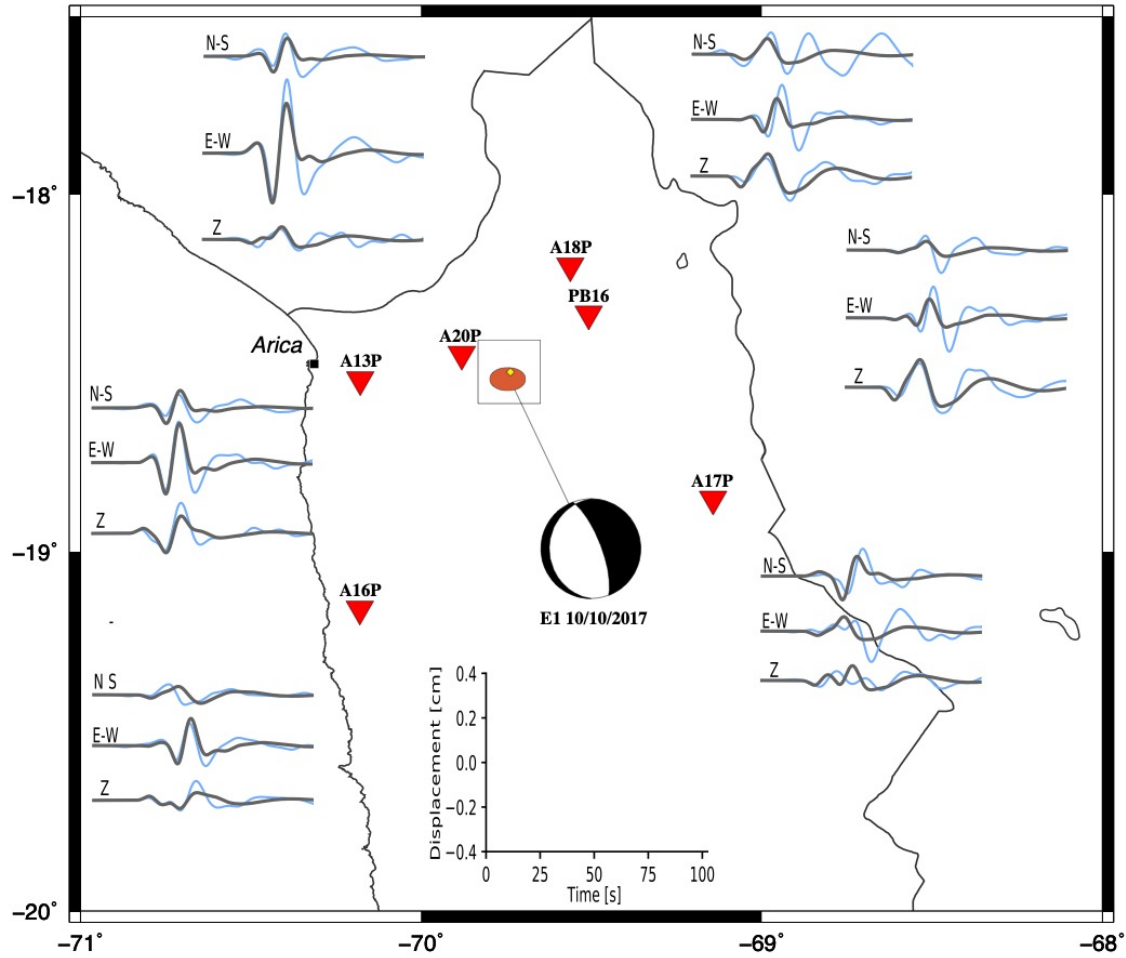
**Figure 5.** Example of kinematic inversion for E1. Ellipse shows the rupture area of the mainshock, with at maximum slip amplitude of 1.08 m. Yellow diamond is the National Seismological Center (CSN) mainshock epicenter. Inverted red triangles are near-field stations considered for inversion. Gray and blue lines are simulated and observed displacement waveforms respectively. Focal mechanism from USGS.

Strength of Oceanic Litosphere

712
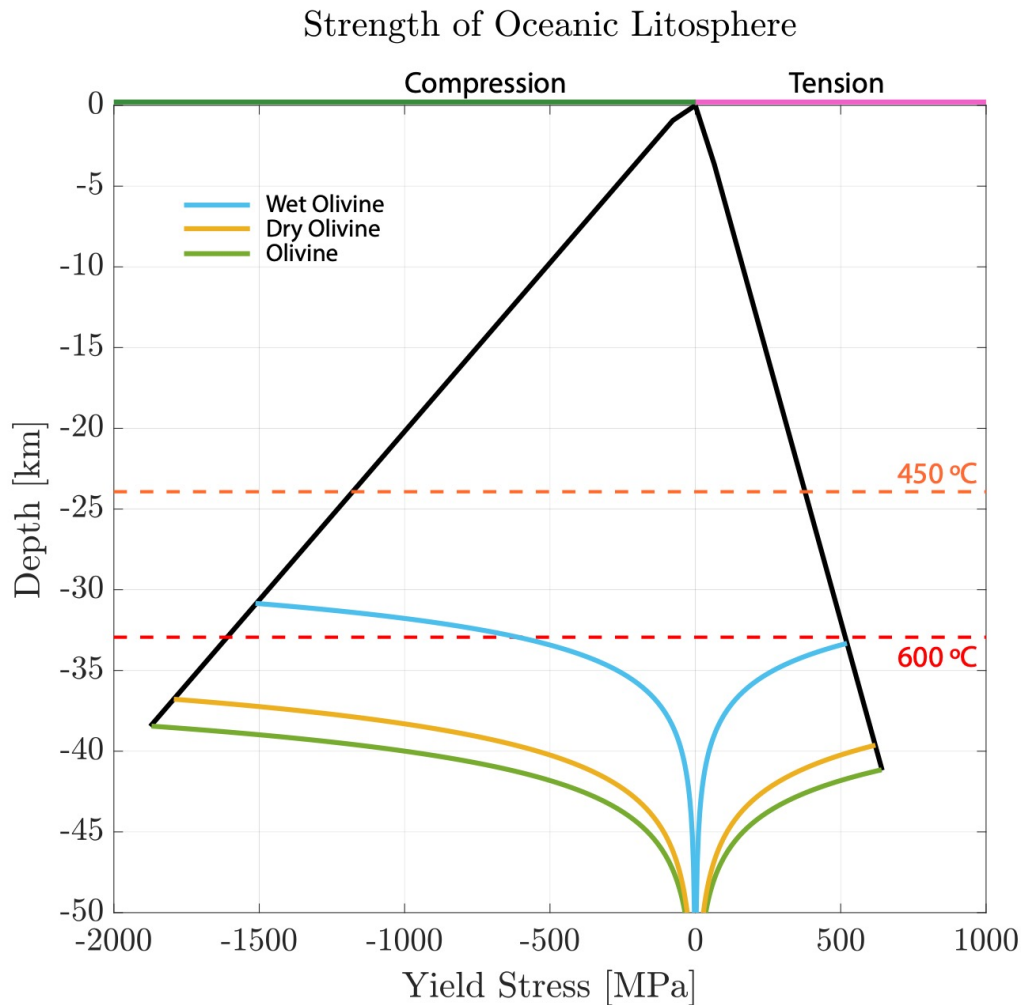
Figure 6. Yield strength envelope for an oceanic lithosphere 58 Myr old. Stress differences or yield stress are limited at the top of
the plate by frictional sliding rule according to Byerlee's frictional sliding rule (black curve). Yield stress is limited at the base of
the plate by steady state creep, which depends on the cube of the stress and exponentially on temperature (Kohlstedt et al., 1995),
and computed considering steady state flow properties for olivine (green line; Goetze, 1978), dry olivine (yellow line; Karato et
al., 1986) and wet olivine (cyan line; Karato et al., 1986). Isotherms were computed based on the cooling of a semi-infinite half-
space mode (Turcotte & Schubert, 2002).

719

720
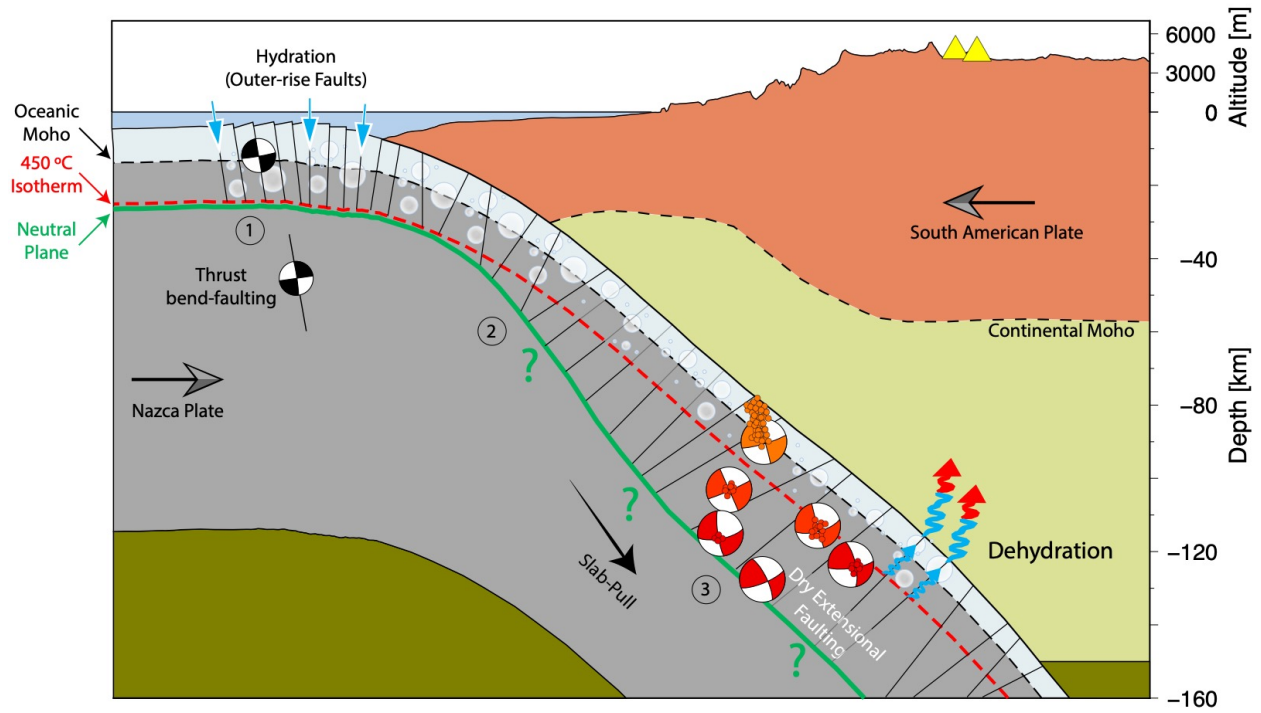
Figure 7. Cartoon showing a conceptual model for the the evolution of subducting lithosphere in northern Chile. The topography of the plate in the outer-rise/trench region has been exaggerated to show better the deformation associated to plate bending. Scale is approximate everywhere else. Bubles in oceanic lithosphere indicate hydration.

724